

Direct Comparison of Anisotropic Damage Mechanics to Fracture Mechanics of Explicit Cracks

John A. Nairn

Wood Science and Engineering, Oregon State University, Corvallis, OR 97330, USA

Tel: +1-541-737-4265

Fax: +1-541-737-3385

Email: John.Nairn@oregonstate.edu

Abstract

Because damage mechanics modeling involves damage initiation followed by propagation that releases energy, it is often uncritically assumed to be an alternative implementation of fracture mechanics. This paper tests that claim by running side-by-side damage mechanics and explicit crack fracture mechanics simulations within the same code on three separate problems. For a center-notched specimen loaded in tension, damage mechanics can reproduce all features of fracture mechanics, but with three restrictions. First, damage mechanics must implement anisotropic damage mechanics rather than simpler isotropic or scalar damage methods. Second, initiation stress and toughness used in damage mechanics must be calibrated before damage mechanics can reproduce either fracture mechanics or experimental results. Third, damage mechanics properties must scale with absolute size of discretization elements. Two other problems considered were mixed-mode, dynamic fracture and cracking of a brittle coating on a substrate. In each case, anisotropic damage mechanics can be made consistent with fracture mechanics by suitable calibration of properties. An advantage of damage mechanics is its potential to model certain complicated issues better than explicit crack fracture mechanics. Two examples are dealing with a transition to shear failure and modeling of fracture events such as periodic cracking in coatings.

Keywords: Damage Mechanics; Fracture Mechanics; Material Point Method; Computational Mechanics

1. Introduction

While material response to subcritical loading is well modeled by computational mechanics, extensions to numerically model initiation and propagation of failure is more complicated. One approach with convincing results is modeling propagation of existing cracks in elastic materials using fracture mechanics. Methods such as crack closure [1] or J -integral analysis [2] can accurately calculate crack-tip stress intensity factors or energy release rate and use those results to predict crack initiation. When using numerical methods that can grow cracks, such modeling can include crack propagation predictions. Fracture mechanics models have been validated by comparison to experiments.

Nomenclature

A_c	Particle crack area	K_I, K_{II}	Stress intensity factors
ADaM	Anisotropic Damage Mechanics	K_{Ic}, K_{IIc}	Critical stress intensity factors in fracture mechanics
CRAMP	MPM with explicit cracks	$K_{Ic}^{(d)}, K_{IIc}^{(d)}$	Critical stress intensity factors in ADaM
D	Damage tensor	MPM	Material Point Method
D	Crack density	η_n, η_t	Stability scaling factors
d_n, d_{ij}	Damage parameters (0 to 1)	ρ	Density
δ_n, δ_{ij}	Cracking strains	$\boldsymbol{\sigma}$	Stress tensor
E	Modulus	σ_n	Initiation normal stress
$\boldsymbol{\varepsilon}$	Strain tensor	t_c, t_s	Coating and substrate thickness
$\boldsymbol{\varepsilon}_{res}$	residual strain tensor	τ_t	Initiation shear stress
$f_n(\delta), f_n(\delta)$	Normal and shear softening laws	u_n, u_{ij}	Crack opening displacements
\bar{G}_{Ic}	Energy released per unit volume	V_p	Particle volume
$G_{Ic}^{(d)}, G_{IIc}^{(d)}$	Damage mechanics toughness	ν	Poisson's ratio
G_{Ic}, G_{IIc}	Fracture mechanics toughness	Δx_p	Particle size
G_{xy}, G_{xz}	Shear moduli	Δz	Semiwidth of damaged zone
I	Identity tensor		

Fracture mechanics works very well for problems with a single existing crack or multiple, non-interacting cracks. When real world problems start with no cracks or damage evolution results in interacting cracks, computational fracture mechanics modeling can become untenable. A potential failure-modeling alternative is damage mechanics [3]. In brief, damage mechanics introduces an evolving fourth-rank damage tensor (D) into the material's constitutive law between stress ($\boldsymbol{\sigma}$) and strain ($\boldsymbol{\varepsilon}$):

$$\boldsymbol{\sigma} = (\mathbf{I} - \mathbf{D})\mathbf{C}_0(\boldsymbol{\varepsilon} - \boldsymbol{\varepsilon}_{res}) \quad (1)$$

where \mathbf{C}_0 is the undamaged material's fourth-rank stiffness tensor and $\boldsymbol{\varepsilon}_{res}$ is a residual strain (such as $\boldsymbol{\varepsilon}_{res} = \boldsymbol{\alpha}\Delta T$ for residual thermal strain due to temperature change ΔT with thermal expansion tensor $\boldsymbol{\alpha}$). Damage mechanics can start without initial cracks (and $\mathbf{D} = 0$) and predict their initiation and orientation using various damage initiation criteria. But this initiation only starts failure. Following initiation, damage evolves with final failure occurring only after dissipation of energy equal to the material's toughness. A connection between energy dissipated in damage mechanics and critical energy release rate in fracture mechanics is typically cited as evidence that damage mechanics is equivalent to fracture mechanics. But such claims are rarely validated by quantitative comparisons between damage mechanics and fracture mechanics models.

Two damage mechanics methods are isotropic damage mechanics and anisotropic damage mechanics. In isotropic damage mechanics, D is replaced by $d_I \mathbf{I}$ where d_I is a "scalar" damage

parameter that evolves from 0 at initiation to 1 at final failure [4, 5]. In isotropic damage mechanics, damage evolution leads to softening in all directions (or all elements of C_0 , see Eq. (1)), but that is a very poor description of failure. Most failure proceeds by coalescence of damage into a crack that causes the material to become anisotropic. For example, the tensile modulus normal to the crack will be lower than tensile moduli parallel to the crack. These fundamental problems with isotropic damage mechanics are potentially resolved by extension to anisotropic damage mechanics, referred to here as ADaM. For example Chaboche *et al.* [6, 7, 8] proposes an anisotropic D that depends on three damage parameters — d_n for damage normal to the cracks and d_{xy} and d_{xz} for shear damage transverse to the crack. Their proposed D leads to softening in modulus normal to the crack and in two shear moduli parallel to the crack plane. After damage, an initially isotropic material becomes an orthotropic material.

ADaM has several other features that recommend it as the preferred damage mechanics method. First, the three damage parameters can be connected to three components of crack opening displacement [9]. In other words, ADaM can model a so-called “strong discontinuity” that physically represents a real crack [4, 5]. Second, normal and shear damage parameters can partition dissipated energy into tensile (mode I) and shear (modes II and III) damage energy. Such a partitioning is a prerequisite for modeling mixed-mode failure. Third, the ability to track crack opening displacement means ADaM can account for crack surface contact if damaged zones are unloaded after damage initiation. Isotropic damage mechanics lacks these features. A single damage parameter can neither track crack-opening displacement vector nor partition energy into normal and shear components. Isotropic damage mechanics has more in common with softening plasticity theory than fracture mechanics [4, 5]. ADaM, however, goes beyond softening plasticity giving it potential as an alternative to fracture mechanics.

This paper uses implementations of both anisotropic damage mechanics [9] and explicit crack fracture mechanics [10] within the same computational mechanics code and runs direct comparisons between the two methods. Three problems were considered — mode I crack propagation in a center-notched specimen, mixed-mode dynamic crack propagation, and cracking of a brittle coating on a substrate. The first two were conventional fracture mechanics problems. ADaM modeling can reproduce fracture mechanics predictions provided ADaM failure properties are calibrated to match. The “toughness” and “strength” needed for ADaM modeling differ from experimental toughness and strength values. The ADaM toughness must be lower than experimental fracture mechanics toughness to account for ADaM describing damage energy over a finite volume while fracture mechanics interprets toughness as energy per unit fracture area. The ADaM strength describes *initiation* of failure in a region of stress concentration that is physically distinct from experimental failure stress. Furthermore, ADaM properties must scale with resolution otherwise damage mechanics predictions would be inconsistent with scaling effects inherent in fracture mechanics. The third, coating/substrate example is a problem that starts without cracks. ADaM can predict initiation and development of multiple cracks in the coating that are consistent with many experimental results and with energy models for predicting cracking as a function of coating thickness.

2. Numerical Methods

All results here used the Material Point Method (MPM), which is a solid mechanics numerical tool that is well suited for solving problems with large deformations, history- and orientation-dependent damage, and contact [11, 12]. MPM is a hybrid Eulerian-Lagrangian formulation where a modeled object is discretized into material points or particles. Information needed to solve equations of motion is extrapolated back and forth between material points and a background grid each time step. This work selected MPM because it has implementations of both explicit crack propagation in arbitrary directions [10] and anisotropic damage mechanics [9]. Although all numerical calculations used MPM, this work’s findings are general and apply to comparisons between fracture mechanics and damage mechanics in both MPM and finite element analysis (FEA). Calculations involving “particles” (or the material points) in MPM correspond to calculations involving “elements” in FEA. This section briefly describes explicit crack and damage mechanics modeling in MPM.

Explicit cracks can be modeled in MPM using the CRAMP (for “CRACKs in MP(M)”) algorithm [10]. In brief, CRAMP extends MPM by introducing crack surfaces whose geometry is defined by a collection of massless particles (in 2D, crack particles connect to define a crack path). When extrapolating between material points and the background grid, the crack geometry is used to partition velocity on the grid into separate velocity fields above and below the crack surface. With these two velocity fields, MPM explicitly models the crack discontinuity [10], can implement contact [13, 14] or traction laws [15] on crack surfaces, and can find crack tip parameters such as J integral [16, 17]. The CRAMP extension of MPM is analogous to XFEM extension of FEA to implement crack discontinuities [18, 19]. Because crack particles work well in the particle-based MPM, CRAMP is a more natural extension of MPM than XFEM is of FEA. Unlike XFEM, CRAMP does not need to modify any shape functions, does not need any assumptions about crack-tip stress state, and can rigorously handle two interacting cracks in the same background grid cell.

To model explicit, mixed-mode crack propagation in 2D problems considered here, total J integral is partitioned into mode I and mode II stress intensity factors (K_I and K_{II}) [16, 17]. The partitioning is done by tracking crack opening displacements using the two grid velocity fields. Mixed-mode crack propagation requires two criteria — a criterion to predict crack initiation and a method to determine its propagation direction. These simulations used the maximum hoop stress (or maximum energy release) criterion where a crack is predicted to propagate in the maximum hoop stress direction (equivalently maximum mode I stress intensity factor direction) [20]. The angle from crack direction to maximum hoop stress direction is [20]:

$$\cos \theta = \frac{3R^2 + \sqrt{1 + 8R^2}}{1 + 9R^2}, \quad \sin \theta = -R(3 \cos \theta - 1), \quad \text{and} \quad R = \frac{K_{II}}{|K_I|} \quad (2)$$

The mode I stress intensity factor in the hoop direction is [20]:

$$K_{I\theta} = \cos \frac{\theta}{2} \left(K_I \cos^2 \frac{\theta}{2} - \frac{3}{2} K_{II} \sin \theta \right) \quad (3)$$

The maximum hoop stress criterion predicts crack propagation occurs when $K_{I\theta}$ equals the material’s mode I critical stress intensity toughness (K_{Ic}) and that crack propagation is in the

θ direction. An alternate criterion is to assume crack growth in direction where $K_{II\theta} = 0$; this approach would have similar predictions to the maximum hoop stress direction used here. In CRAMP, a crack propagates by adding a crack particle ahead of the crack tip at angle θ to the crack plane at a distance equal to MPM particle size. A special case for mode I fracture (where $K_{II} = 0$) models crack propagation when $K_{I\theta} = K_I = K_{Ic}$ by self-similar propagation ($\theta = 0$).

The damage mechanics (or ADaM) simulations here used the recent MPM implementation described in Ref. [9] that uses the anisotropic D proposed by Chaboche *et al.* [6, 7, 8]. In brief, an initially isotropic material loads elastically until a principle stress exceeds its tensile initiation stress (σ_n) or until maximum shear stress exceeds its shear initiation stress (τ_t). Once damage initiates, a particle is marked as damaged with a complete crack spanning its entire cross-section. The crack normal and its area within the particle (A_c) are determined by principle stress directions and failure mode. The crack normal provides a one-to-one correspondence between damage variables ($d_n, d_{xy},$ and d_{xz}) and three components of the crack-opening displacement vector ($\mathbf{u} = (u_n, u_{xy}, u_{xz})$) [9]. Within the crack axis system (coordinate system with crack normal in the x direction), the material becomes orthotropic with reduced tensile modulus normal to the crack (E_{xx}) and reduced shear moduli tangential to the crack (G_{xy} and G_{xz}). The damage mechanics properties needed for initiation, damage evolution, and failure are:

1. Two initiation stresses — σ_n and τ_t to initiate tensile or shear failure.
2. Evolve three cracking strains — $(\delta_n, \delta_{xy}, \delta_{xz}) = A_c \mathbf{u} / V_p$ where V_p is particle volume and A_c is crack surface area in the particle.
3. Two softening laws — $f_n(\delta_n)$ to characterize how crack normal opening affects damage and $f_t(\delta_{ij})$ to characterize how tangential crack sliding (in 2D) or two tangential sliding directions (in 3D) affect damage. Note that 3D simulations have two shear damage variables that can express different levels of damage in the two orthogonal shear directions, but by material isotropy, they use the same softening law. All simulations here used linear softening laws.

The softening laws are made dimensionless and monotonic such that they decrease from $f(0) = 1$ to $f(\delta_c) = 0$ at some critical crack-opening strain. Damage evolution is determined by limiting crack tractions to $\sigma_n f_n(\delta_n)$ and $\tau_t f_t(\delta_{ij})$ [9]. The area under the full softening law is energy dissipated per unit volume, \overline{G}_{Ic} . It is related to damage mechanics energy released per unit area, $G_{Ic}^{(d)}$, by scaling by the V_p/A_c ratio:

$$G_{Ic}^{(d)} = \frac{V_p}{A_c} \overline{G}_{Ic} = \frac{V_p \sigma_n}{A_c} \int_0^{\delta_{nc}} f_n(\delta) d\delta = \int_0^{u_{n,crit}} \sigma_n f_n(u_n) du_n \quad (4)$$

where $u_{n,crit}$ is the critical crack-opening displacement. In other words, $G_{Ic}^{(d)}$ is area under dimensioned softening law within a particle as a function of particle crack-opening displacements. Analogous expressions hold for shear toughness, $G_{IIc}^{(d)}$.

ADaM models a “strong discontinuity” [4, 5] and tracks crack opening displacements. This modeling allows ADaM to model mixed-mode failure with separate properties for mode I and

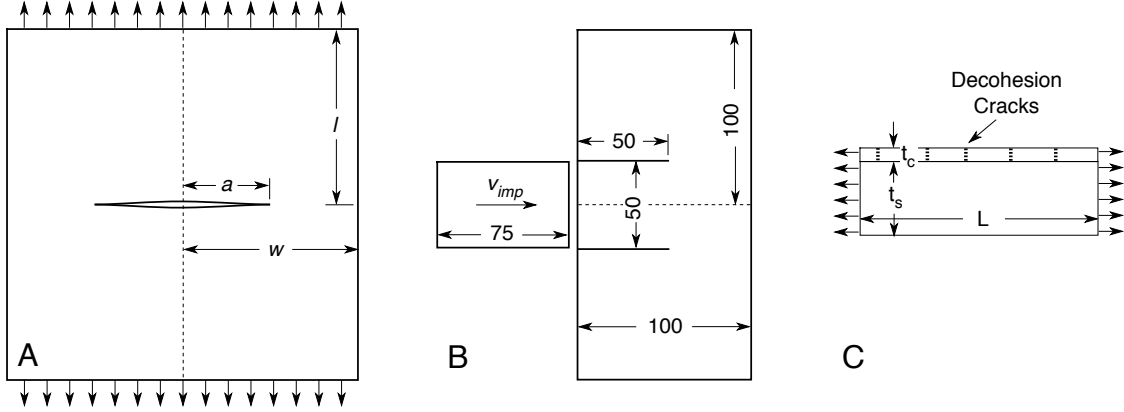


Figure 1: A. Center-notch specimen loaded in tension. The right half of the specimen was modeled by symmetry. B. Edged notch specimen loaded by impact between two notches with a impactor whose width equals the distance between notches. The top half of the specimen was modeled by symmetry. C: Coating/substrate specimen loading by axial tension.

mode II toughness. Modeling of mixed-mode failure used an elliptical failure criterion such that 2D failure occurs when:

$$\left(\frac{G_I}{G_{Ic}^{(d)}} \right)^2 + \left(\frac{G_{II}}{G_{IIc}^{(d)}} \right)^2 = 1 \quad (5)$$

where G_I and G_{II} are determined from energy released up to current crack-opening displacement and $G_{Ic}^{(d)}$ and $G_{IIc}^{(d)}$ are two damage mechanics toughness properties [9]. Finally, stability in damage mechanics requires sufficient spatial resolution. As derived in Ref. [9], particle linear dimensions, Δx_p (or element dimensions in FEA), must satisfy

$$\Delta x_p < \min \left(\eta_n \left(\frac{K_{Ic}^{(d)}}{\sigma_n} \right)^2, \eta_t \left(\frac{K_{IIc}^{(d)}}{\tau_t} \right)^2 \right) \quad (6)$$

where η_n and η_t depend on the softening law. The squared ratios of critical stress intensity factor ($K_{Ic}^{(d)}$ or $K_{IIc}^{(d)}$) to strength (σ_n and τ_t) have units of length and scale with crack-tip, damage zone size [21, 22]. This stability condition shows that modeling brittle materials with small damage zones requires higher resolution than modeling ductile materials. The η factors are equal to 2 for linear softening. Furthermore they are maximized for linear softening, which means linear softening is the most stable damage mechanics softening law [9]. Some seemingly-reasonable softening laws should be avoided because they are always unstable (e.g., power-law softening).

3. Results

Three examples shown in Fig. 1 were used to compare fracture mechanics using CRAMP to anisotropic damage mechanics using ADaM.

3.1. Center-Notched Specimens in Tension

Figure 1A shows a tension-loaded, center-notched specimen (CNT). The modeled material was aluminum with elastic properties $E = 74$ GPa, $\nu = 0.34$, and $\rho = 2.78$ g/cm³. Typical mode I failure properties for aluminum are $G_{Ic} = 8$ kJ/m² ($K_{Ic} = 25.87$ MPa $\sqrt{\text{m}}$) [23] and tensile strength $\sigma_{max} = 300$ MPa. The specimen was loaded at a constant displacement rate such that an aluminum stress wave (with $v_{wave} = 5159$ m/s) would make n transits across specimen length by the time the specimen is loaded to 1% strain. This timing corresponds to a displacement rate equal to $1/(2n)$ percent of the material's wave speed. The value of n was increased until stress-strain curves approximated quasi-static conditions as evidenced by simulated failure using fracture mechanics modeling agreeing with quasi-static fracture predictions. A value of $n = 25$ was sufficiently slow and corresponds to displacement rate of 0.02% of the material's wave speed. Each MPM simulation modeled the right half the specimen with symmetry conditions along the midplane. All 2D simulations used a regular background mesh with square cells and four particles per cell.

A CRAMP simulation for crack length as function of time for a specimen with $l = w = 50$ mm and $a/W = 0.51$ using 1 mm cells in the background mesh (or 0.5 mm particles) is given in Fig. 2 (dashed curve). When cell size was varied from 0.25 mm cells to 5 mm cells both initiation time and crack propagation speed remained constant, which indicates fast convergence. Because explicit crack propagation is done in discrete increments equal to particle size, low-resolution crack length curves had a "stair-step" appearance. A 1 mm cell size was chosen for reference simulations because crack growth curves were relatively smooth. Convergence was also confirmed by comparing simulated maximum stress, which was $\sigma_{max} = 77.2$ MPa, to fracture mechanics result of [21]:

$$\sigma_{max} = \frac{K_{Ic}}{Y(a/W)\sqrt{\pi a}} \quad (7)$$

where $Y(a/W)$ is fracture mechanics calibration function for CNT specimen with $l/w = 1$ and uniform displacement loading. $Y(a/W)$ was calculated using finite element crack closure methods [24] resulting in $Y(0.51) = 1.18$ leading to fracture mechanics result of $\sigma_{max} = 77.5$ MPa.

For ADaM modeling, mode I crack growth depends on $G_{Ic}^{(d)}$, σ_n , and the linear softening law $f_n(\delta_n)$ (mode II properties were not needed). Figure 2 illustrates the process of comparing ADaM properties to fracture mechanics predictions. The ADaM curves plot extent of failure by tracking positions of failed materials points (decohesion by Eq. (5)) that develop starting at the tip of an explicit (but non-propagating) crack. In other words, CRAMP was used to introduce an explicit crack, but ADaM and crack tip stress state modeled the crack propagation. First, a reasonable σ_n value was selected and $G_{Ic}^{(d)}$ was varied. Choosing $G_{Ic}^{(d)} = G_{Ic}$ significantly differed from fracture mechanics. The explanation is that damage mechanics dissipates energy over a damaged volume of particles in the crack path; the dissipated energy per unit volume is \bar{G}_{Ic} in Eq. (4). If we assume the damage volume extends a distance Δz on either side of the crack plane, equating total dissipated ADaM energy ($\bar{G}_{Ic} \times (\text{damage volume})$) to total fracture

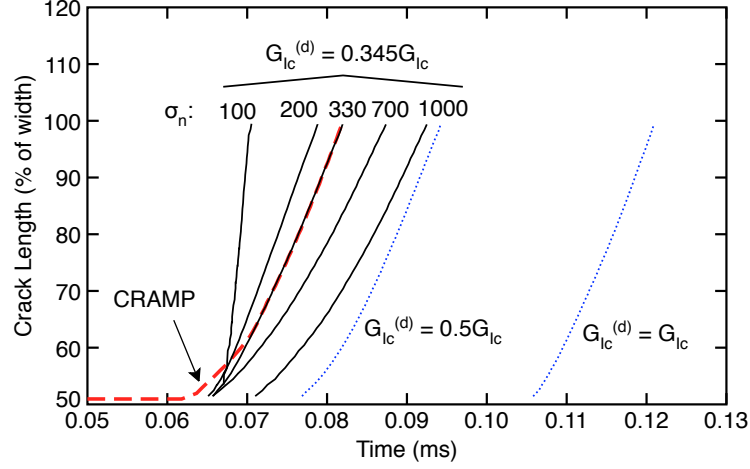


Figure 2: Comparison of explicit fracture mechanics crack propagation by CRAMP modeling (thick dashed line) with $G_{Ic} = 8 \text{ kJ/m}^2$ to several ADaM simulations with various values for $G_{Ic}^{(d)}$ and σ_n .

mechanics energy ($G_{Ic} \times (\text{crack area } A)$) and using $V_p/A_c \sim \Delta x_p$, leads to:

$$\bar{G}_{Ic} 2A \Delta z = G_{Ic}^{(d)} \frac{A_c}{V_p} 2A \Delta z = G_{Ic} A \quad \text{or} \quad G_{Ic}^{(d)} \sim G_{Ic} \frac{\Delta x_p}{2\Delta z} \quad (8)$$

All simulations damaged at least one particle on each side of the crack plane suggesting $\Delta z \geq \Delta x_p$ and $G_{Ic}^{(d)} \leq 0.5 G_{Ic}$. A more precise scaling was determined by fitting ADaM predictions to fracture mechanics models. The main effect of varying $G_{Ic}^{(d)}$ was to shift crack initiation time; setting $G_{Ic}^{(d)} = 0.354 G_{Ic}$ led to damage mechanics simulations that matched fracture mechanics initiation time. To refine the fit, damage initiation stress, σ_n , was varied from 100 to 1000 MPa (see Fig. 2). This variation predominantly changed crack growth rate, but could affect initiation time (see $\sigma_n = 1000$ MPa curve). A best fit was found for $\sigma_n = 330$ MPa and $G_{Ic}^{(d)} = 0.354 G_{Ic}$.

In summary, by calibrating ADaM properties, damage mechanics models can be made to agree with fracture mechanics in virtually all features. The crack growth rates matched well as did the full stress-strain curves (see Fig. 3) and specimen stress distributions [9]. Importantly, ADaM properties *differ* from aluminum failure properties. $G_{Ic}^{(d)}$ had to be scaled down to account for damage volume in damage mechanics *vs.* energy per unit area in fracture mechanics. Initiation stress, σ_n , was determined by fitting to fracture mechanics modeling and therefore had no relation to experimental strength of aluminum (although coincidentally, this first initiation stress was close to its strength).

Consider this thought experiment — imagine a series of geometrically identical CNT specimens (*i.e.*, l/w and a/w constant) with varying absolute widths. Elasticity analysis of such specimens reveals that stress distributions as a function of non-dimensional x/w and y/w are independent of specimen size. Fracture mechanics predictions of failure, however, depend on size because stress intensity factor scales with absolute crack length. Now construct some numerical failure model as an alternative to fracture mechanics. If that model is based on a

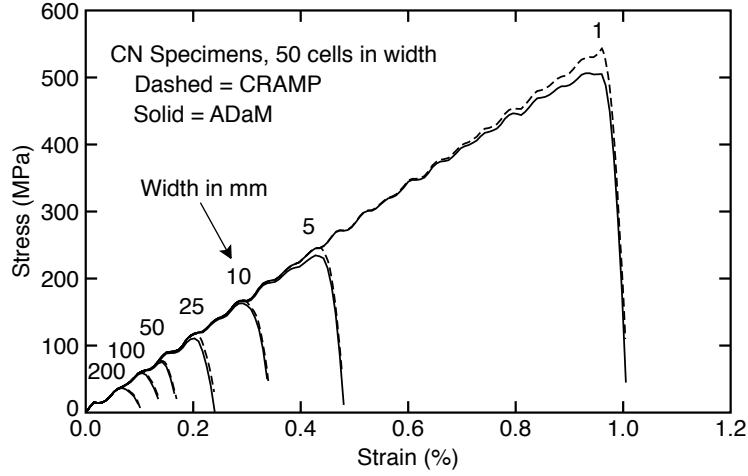


Figure 3: Predicted stress strain curves for CRAMP modeling (dashed lines) compared to ADaM modeling (solid curves) as a function of specimen width (as indicated) in mm. The oscillations are small dynamic effects, but the loading rate was slow enough that transients never caused failure and the peak load agreed with quasi-static fracture mechanics predictions.

stress-based criterion with input material properties that do not scale with absolute size, such a numerical model *would never agree* with fracture mechanics. Fortunately, ADaM is not purely a stress-based failure model. Although stress state is used to initiate damage, damage evolution is controlled by energy dissipated per unit volume. As discussed in Ref. [9] (and shown in Eq. (4)), for constant input $G_c^{(d)}$, energy dissipation per unit volume scales with particle size.

To test ADaM scaling, a series of CNT specimens with $l = w$ ranging from 1 to 200 mm were analyzed. All specimens used 50 cells across the width leading to cell sizes ranging from 0.02 to 4 mm and all were loaded at a displacement rate equal to 0.02% of the material's wave speed. The triangular symbols in Fig. 4 plot ADaM failure load as a function of cell size when using properties determined by fitting fracture mechanics for a 50 mm specimen ($\sigma_n = 330$ MPa and $G_{Ic}^{(d)} = 0.354G_{Ic}$). Although failure load changed with specimen width, it did not match fracture mechanics predictions (solid line labeled σ_{max}). The smallest 1 mm specimen never fully damaged. The problem is that for constant σ_n and $G_{Ic}^{(d)}$, the critical crack opening displacement at failure ($u_{crit} = 2G_{Ic}^{(d)}/\sigma_n$ for linear softening) is also constant. To reach u_{crit} , the crack-opening strain must reach $u_{crit}/\Delta x_p$. For very small Δx_p , the required strain is not reached prior to large-strain, crack-tip, numerical instabilities.

Two explanations are possible. First, ADaM may be giving the correct response to short cracks. Fracture mechanics is known to eventually break down for short cracks [25] and perhaps damage mechanics is realistically modeling a transition to different failure modes for short cracks. Second, fracture mechanics is the correct model for elastic failure implying that ADaM must change σ_n and/or $G_{Ic}^{(d)}$ with particle size to replicate fracture mechanics. The required ADaM property changes for this second option were found by fitting to CRAMP simulations as described above. The best-fit σ_n as function of cell size is plotted in Fig. 4. The power-law fit has a slope of -0.49 that is caused by characteristic $1/\sqrt{r}$ dependence in crack

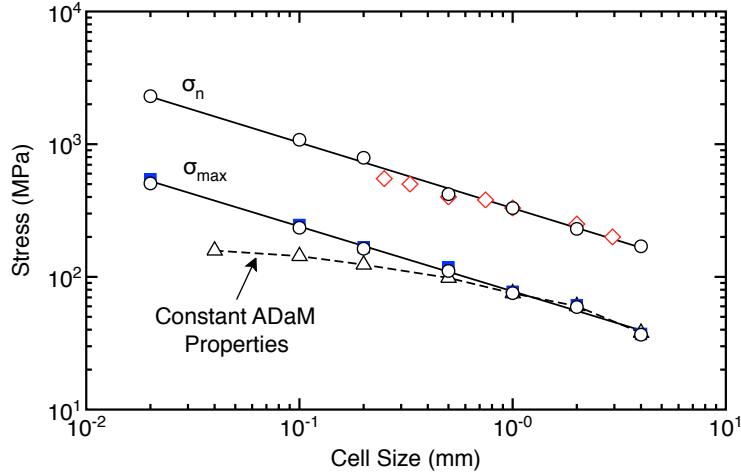


Figure 4: Initiation stress, σ_n , and final failure stress, σ_{max} , for aluminum CNT specimens as a function of cell size. The triangles are ADaM results with constant $\sigma_n = 330$ MPa and $G_{Ic}^{(d)} = 0.354G_{Ic}$; the open circles are ADaM simulations with variable properties; the solid squares are CRAMP results. These results all varied cell size by changing absolute width specimen. The diamonds are for a 50 mm CNT specimen where cell size was changed by varying the resolution.

tip stress state [22]. All calibrated ADaM simulations agreed well with fracture mechanics predictions as demonstrated by matching stress strain curves in Fig. 3. The maximum stresses, σ_{max} , from stress-strain curves are plotted in Fig. 4; ADaM and CRAMP were virtually identical and agreed with fracture mechanics in Eq. (7). The best-fit $G_{Ic}^{(d)}$ increased slightly for smaller specimens, but except for the smallest 1 mm specimen (20 μm cells), $G_{Ic}^{(d)} = (0.36 \pm 0.03)G_{Ic}$ over a 100-fold change in cell size.

A second scaling test kept specimen width constant ($w = 50$ mm) but varied particle size (*i.e.*, varied resolution). Figure 4 (diamond-shaped symbols) plots the σ_n needed to match fracture mechanics. These results are plotting the effect of cell size on σ_n for constant width but variable resolution. The trend matches previous results for effect of cell size at variable width but constant resolution (circles). The resolution results did not continue to smallest cell size because the total number of particles made the problem too large for practical, manual calibration of properties. In practice, simulations of this specimen would not need 0.2 mm cells (or 200 cells across the specimen width) to resolve crack tip details, but all results show that properties do need to scale with particle size for both changes in resolution and changes in absolute specimen size.

The above ADaM simulations used CRAMP to introduce an explicit crack and ADaM to predict propagation. The same problem can also be modeled entirely using damage mechanics by modeling the crack with a line of fully damaged particles when the simulation begins. Such simulations gave results identical to above simulations provided that the initially damaged particles spanned the width of an entire cell in the background grid. In other words, in MPM modeling with 2 particles across width of each cell, the initial crack requires a path of failed particles at least two particles wide.

In summary, ADaM properties differ from material toughness and strength and they must scale with particle size. For aluminum modeling, best-fit ADaM properties in mode I were $\sigma_n \sim 330/\sqrt{2\Delta x_p}$ MPa and $G_{Ic}^{(d)} \sim 0.36G_{Ic} = 2880 \text{ J/m}^2$. All these simulations used a regular grid with equally-sized particles having the same ADaM properties. In contrast, FEA models that use variably-sized elements in an effort to resolve some areas more than others (or MPM modeling with variable size particles), must vary ADaM properties within the same simulation depending on element (or particle) size. Without such scaling, the model will not correctly predict damage propagation that moves between areas in the model having different resolution. Scaling rules determined here were for square elements. The scaling for rectangular or arbitrary, isoparametric elements may differ.

3.2. Mixed Mode Simulation Compared to Experiments

Figure 1B shows a double-edge notched specimen impacted with a cylindrical projectile whose diameter matches the distance between the two cracks. Selected experiments with this configuration are described by Kahlhoff and Winkler [26, 27] and their results have been the subject of several numerical investigations [28, 29, 30]. The projectile was fired with air gun velocities ranging from 10 m/s to 100 m/s. The specimen was 100×200 mm with two 50 mm cracks separated by 50 mm. The fracture experiments were done on high-strength steel. No steel properties were provided; these simulations used typical high-strength steel properties $E = 190,000 \text{ MPa}$, $\nu = 0.3$, and $\rho = 7.83 \text{ g/cm}^3$. The experimental papers [26, 27] specified neither length nor mass of the steel projectile. Assuming a figure in Ref. [27] was drawn to scale, the projectile was estimated to be 75 mm in length. To model using 2D simulations, projectile density was adjusted such that mass of the modeled $75 \times 50 \text{ mm}$ rectangular slab had the same total mass as a 75 mm long cylinder. The simulations modeled the top half of the specimen using midplane symmetry. Both experiments and simulations impacted a free-floating specimen or a specimen not held by any fixtures or boundary conditions.

The experiments were done on specimens prepared with different notch radii and concluded that observations scale with v_{imp}/\sqrt{r} where v_{imp} is impact velocity and r is notch-tip radius [26, 27]. Some experiments were labeled “precracked” and meant to be sharp cracks (with estimated $r = 0.2 \text{ mm}$ [26, 27]). The simulations done here did not attempt to resolve notch-tip radius effects and therefore focused on sharp-crack results. A summary of experimental observations scaled to sharp cracks conditions [26, 27] follows:

1. At low velocity, impact causes no crack propagation, but at a critical velocity of about 10 m/s, it suddenly causes a full crack (*i.e.*, complete specimen failure) with initial crack growth at about 70° to the initial notch direction.
2. For velocities above about 20 m/s, failure transitions to shear failure.
3. After the transition, impacts cause incomplete shear failure with the shear cracks “in a direction which is almost identical with the original direction of the notch,” but “inclined by a small angle” toward the specimen midplane [27]. The shear damage increases in length until becoming a full crack through the specimen at about 40 m/s.

These crack-length “observations” as a function of impact velocity are plotted in Fig. 5.

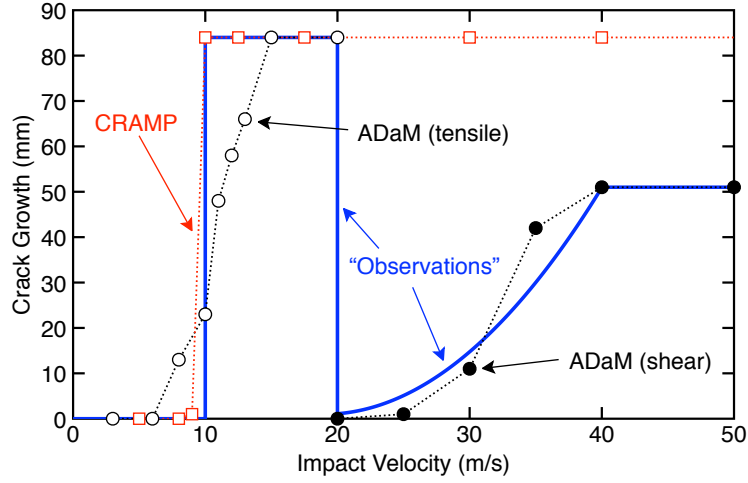


Figure 5: Final crack growth for double-edge notched specimens loaded in impact as a function of impact velocity. The thick solid curves are idealized experimental “observations”; the open squares are CRAMP results; the open circles are ADaM simulations using mode I failure properties; the solid circles are ADaM simulations assuming shear strength decreased and $G_{Ic}^{(d)}$ increased at impact velocity of 20 m/s.

CRAMP simulations for this specimen used 1 mm cells (or 0.5 mm particles). The steel toughness was determined by varying K_{Ic} until no crack growth was observed below the experimental initiation at $v_{imp} = 10$ m/s. The numerically-determined, plane-strain toughness was $K_{Ic} = 37 \text{ MPa}\sqrt{\text{m}}$ (or $G_{Ic} = 6557 \text{ J/m}^2$). The predicted crack angle started at 70° and then decreased slightly as crack propagation developed (see Fig. 6). The experimental result of 70° was determined from “only the beginning of the crack path” [27] and therefore matched the CRAMP modeling. Simulations at other resolutions confirmed that 1 mm cells provided converged results. All subsequent ADaM simulations used this same resolution.

The observed crack growth at 70° is characteristic of a mode I failure path for a crack subjected to mode II loading. By maximum hoop stress criterion, pure mode II loading has

$$\lim_{K_I \rightarrow 0} \cos \theta = \frac{1}{3} \quad \text{or} \quad \theta = 70.5^\circ \quad (9)$$

In other words, the maximum hoop stress criterion in explicit crack modeling should inevitably get crack growth at close to 70° . ADaM modeling, however, has no direction criterion. The direction is controlled by initiation criterion, which here used principle stress directions. To test ADaM simulation of angled cracks, the first simulations focused on mode I damage mechanics properties. Again, $G_{Ic}^{(d)}$ had to be less than $0.5G_{Ic}$ to observe transition to crack initiation around $v_{imp} = 10$ m/s. For fixed $G_{Ic}^{(d)}$, changes in σ_n had two effects. First, crack angle increased from about 60° to 85° as σ_n increased from 500 to 1500 MPa. Second, if σ_n was too low, dynamic stress waves caused crack initiation on the free edge opposite the impact that propagated along the specimen midplane. Once a midplane crack formed, the angled crack propagation stopped. With $G_{Ic}^{(d)} = 0.5G_{Ic}$, σ_n had to be 800 to 1000 MPa to reproduce observed crack angle, but this stress was too low to prevent midplane cracking. By decreasing $G_{Ic}^{(d)}$ to

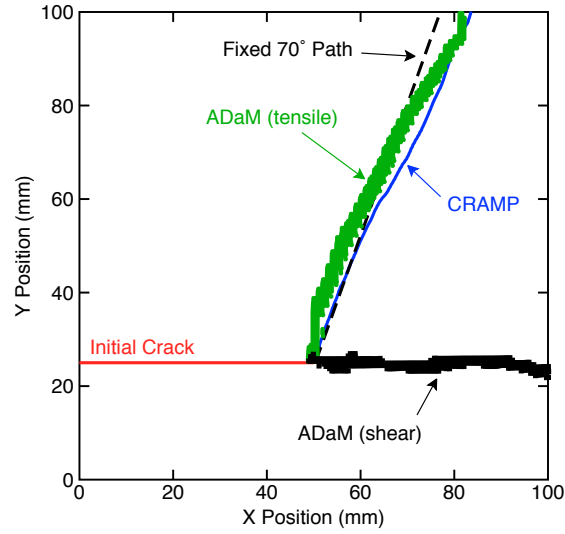


Figure 6: The crack propagation paths predicted by CRAMP modeling (solid line), by ADaM tensile failure simulations, and by ADaM simulations with shear failure (solid symbols). For reference, the dashed line shows a 70° crack that corresponds to the initial crack direction observed in experiments at impact velocity below 20 m/s.

$0.3G_{Ic}$ and using $\sigma_n = 1200$ MPa, ADaM gave a single angled crack close to the experimental angle. The initial ADaM crack angle was higher than 70°, but overall averaged about 70° (see Fig. 6). Because the damage process turned from the initial crack to the mode I stress direction, as long as mode II properties had $\tau_t > 0.5\sigma_n = 600$ MPa and $G_{IIc}^{(d)} > G_{Ic}$, failure was dominated by mode I damage and results were unaffected by mode II properties.

Figure 5 plots final crack length as a function of impact velocity for both CRAMP (open squares) and mode I failure using ADaM (open circles) simulations as a function of impact velocity. The CRAMP simulations, like experimental results, had an abrupt change from no crack growth to complete failure by an angled cracks at $v_{imp} > 10$ m/s. The crack angle decreased to about 62° at $v_{imp} = 40$ m/s, but never switched to shear cracks as observed in experiments [26, 27]. Mode I ADaM simulations also had a transition to complete failure around $v_{imp} = 10$ m/s, but it was more gradual than for CRAMP — failure started with $v_{imp} = 8$ m/s and did not reach failure until $v_{imp} = 15$ /ms. For $v_{imp} > 20$ m/s, mode I ADaM simulations continued to show a dominant crack at angles around 70°. The highest velocity started to develop horizontal branches off the main crack. While appearance of branching at high velocities is potentially interesting, no branched was mentioned in experiments [26, 27].

Neither CRAMP nor ADaM can predict a transition to shear failure at $v_{imp} = 20$ m/s. Fracture mechanics modeling would require proposing new mixed-mode criteria for failure load and direction at higher impact velocity. But, how or why should these change? Similarly, ADaM modeling would require rate-dependent damage properties, but maybe only small changes would be needed? The next ADaM simulations attempted to fit experimental observations by changing just $G_{IIc}^{(d)}$, and τ_t while keeping mode I properties fixed. While these simulations showed shear cracks, they did not arrest the angled crack. For simulations consistent with experiments, $G_{Ic}^{(d)}$ was increased until shear failure dominated the damage process and then

$G_{IIc}^{(d)}$, and τ_t were varied to match experimental results. The solid circles in Fig. 5 compare ADaM crack propagation to experimental observations by using $G_{Ic}^{(d)} = 2G_{Ic}$, $G_{IIc}^{(d)} = 5.7G_{Ic}$, and $\tau_t = 500$ MPa (σ_n was kept constant at 1200 MPa). With these properties, predicted crack length vs. impact velocity tracked observations well (see Fig. 5). Predicted shear cracks were in the direction of the original crack with a slight bend toward sample midplane near the free edge (see Fig. 6). Experimental observations may indicate slightly more inclination toward specimen midplane [26, 27]. Although selected changes in ADaM properties (such as to $G_{IIc}^{(d)} = 3.8G_{Ic}$ and $\tau_t = 425$ MPa) could replicate more inclination toward the midplane, the final failure became coalescence of a crack emanating from the crack tip with a crack that initiated later on free edge of the specimen. The experiments did not have the time resolution needed to determine if shear cracks formed by this process.

In summary, all experimental results can be reproduced by setting $G_{IIc}^{(d)} = 5.7G_{Ic}$ and $\sigma_n = 1200$ MPa while $G_{Ic}^{(d)}$ and τ_t depend on impact velocity. For $v_{imp} < 20$ m/s, $G_{Ic}^{(d)} = 0.3G_{Ic}$ and $\tau_t > 600$ MPa. But for $v_{imp} > 20$ m/s, $G_{Ic}^{(d)}$ increases significantly (to at least $G_{Ic}^{(d)} = 2G_{Ic}$) and τ_t decreases slightly to $\tau_t = 500$ MPa. Certainly ADaM could not *predict* double-edge notched specimen results by input of literature values for toughness and strength of high-speed steel. But, once damage mechanics properties are calibrated by these experiments, one could hope ADaM simulations could predict dynamic fracture of high-speed steel under other loading conditions. With additional experiments, damage mechanics properties and their rate dependences could be refined further. As determined in CNT simulations, these damage mechanics properties for high-speed steel, especially σ_n and τ_t , would need to scale with absolute material points (or element) size.

3.3. Cracking of Coatings and Comparison to Finite Fracture Mechanics

Reference [9] showed that ADaM can predict formation of periodic cracks in brittle coatings that reproduces many features seen in experiments. This section extends that modeling to higher-resolution simulations, to looking at effect of coating thickness, and to compare ADaM predictions to finite fracture mechanics modeling for coating cracks.

Figure 1 shows a coating of thickness t_c (with mechanical properties $E_c = 10$ GPa, $\nu_c = 0.33$, and $\rho_c = 1$ g/cm³) on a substrate of thickness $t_s = 10$ mm (with mechanical properties $E_s = 1$ GPa, $\nu_s = 0.33$, and $\rho_s = 1$ g/cm³). A specimen of length $L = 200$ mm was loaded by displacement control in the x direction up to 2% total strain. To simulate brittle cracking, damage mechanics properties of the coating were set to $\sigma_c = 10$ MPa and $G_{Ic}^{(d)} = 100$ J/m². For simulation of tensile cracking, mode II damage properties had no effect provided $\tau_t > \sigma_n/2$ and $G_{IIc}^{(d)} \gtrsim G_{Ic}^{(d)}$. Figure 7 shows three simulations for $t_c = 2, 3,$ and 4 mm. Each simulation initiated damage throughout the entire coating soon after applied strain reached initiation strain of $\varepsilon_n = \sigma_n/E_c = 0.1\%$. On continued loading, isolated regions failed as “decohesion cracks” (see Fig. 1) that eventually developed into a periodic array of coating cracks. The symbols in Fig. 7 plot crack density as a function of applied strain. All simulations used 0.5 mm cells (0.25 mm particles), which was verified as sufficiently small for convergence. Crack density curves were independent of loading rate providing the rate was less than 2 m/s; all simulations used 1 m/s, which corresponds to 0.1% of the substrate’s tensile wave speed (or

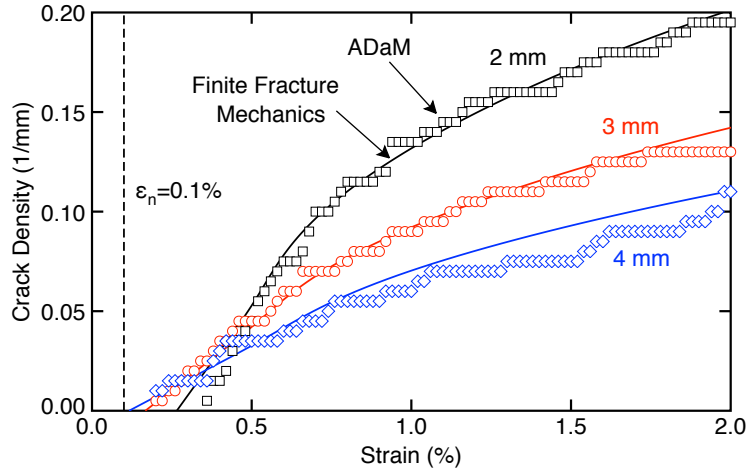


Figure 7: Crack density as a function of applied strain by ADaM simulations (symbols) and as fit to finite fracture mechanics modeling (solid lines). The three curves are for three different coating thicknesses. All ADaM simulations used $\sigma_n = 10$ MPa and $G_{Ic}^{(d)} = 100$ J/m². All finite fracture mechanics fits used $G_{mc} = 500$ J/m² and $f = 1.4$. The vertical dashed line is the assumed ADaM initiation strain.

0.32% of the coating's tensile wave speed). These simulations are an interesting example of predicting localization (*i.e.*, formation of multiple cracks), but it is challenging to speculate on why it worked so well. Presumably, once a particle fails the nearby particles are rapidly induced to fail and a crack propagates across the width of the coating while stress reduction on other particles near the crack plane kept the damage localized. This localization occurs despite the use of homogenous properties. Localization into multiple cracks in other materials might need new numerical methods such as stochastic initiation of failure properties providing weak zones that promote cracks.

ADaM predictions for crack density as a function of applied strain agree with experimental observations on cracking of coatings [31, 32, 33, 34]. Specifically, soon after the first coating crack, crack density increases rapidly. Eventually at higher strain, cracking slows or approaches a saturation crack distribution. Notice that the strain to initiate cracking is 0.40%, 0.24%, and 0.20% for the 2, 3, and 4 mm thick coatings, respectively. All these values are above the damage mechanics initiation strain of $\varepsilon_n = 0.1\%$. While some might be tempted to accept the strain at initiation of cracking as an experimental measure of damage mechanics initiation strain, that approach would be wrong. Damage mechanics initiation strain is when damage starts, but that damage would typically be invisible. The first crack only forms after sufficient energy has been dissipated to fail the particles. This observation is an example of the difference between damage mechanics initiation criteria needed and experimental strength observations as determined by stress at some observed failure.

Because all coating simulations used the same size particles (0.25 mm), damage mechanics properties were kept constant as coating thickness changed. Nevertheless, ADaM simulations predicted scaling effects in cracking of coatings. As coating thickness increased, the strain at crack initiation decreased. At high strain, the saturation crack density decreased for

thicker coatings. These scaling predictions agree with experimental observations on cracking of coatings [31, 32, 33, 34] and on more-extensive cracking observations in layered composites [35, 36, 37]. Any attempt at failure modeling based on crack formation when stress in a layer reaches its strength would never agree with experiments. This short-coming of strength criteria has been confirmed by poor results when strength criteria were used to interpret layer cracking experiments [35, 36, 37]. ADaM's ability to correctly predict scaling is a significant feature that recommends its use for future work on unexplored issues about layer cracking.

Predicting coating cracks is an example problem that relies on initiation criteria. A damage mechanics approach has potential to work on such problems while explicit crack fracture mechanics is hindered by lack of initial cracks. Although conventional fracture mechanics cannot be used and strength-based models always fail to predict scaling effects, cracking of coatings and layers in composites has been successfully modeled by an extension of fracture mechanics to a method termed "finite fracture mechanics" [35, 38, 36, 37]. Finite fracture mechanics is an energy-based method to predict fracture events whereby the next fracture event is predicted to occur when total energy released by that event equals material toughness [31, 39, 34].

Finite fracture mechanics for coatings requires analysis for energy released by each coating crack. The analysis can begin by evaluating effective modulus of the coating/substrate specimen, $E_{eff}(D)$, as a function of current crack density, D , in the coating layer. A variational mechanics analysis results in [31, 39]:

$$\frac{1}{E_{eff}(D)} = \frac{1}{E_0} \left(1 + \frac{2t_c^2 D}{t_c + t_s} \psi(D) \right) \quad (10)$$

where $\psi(D)$ is a dimensionless function.¹ Now imagine a new crack forming between two existing cracks separated by distance $L = f/D$. The factor f is used to account for a distribution of crack spacings. Because the amount of energy released is higher for larger L , each new crack tends to form in regions with higher L implying $f > 1$. Experimental results confirm that $f = 1.25$ to 1.5 provides good approach to accounting for crack distribution effects [35]. The energy release rate for forming a crack in such an interval interval (in the absence of residual stresses as modeled here) is [31, 39]:

$$G_m = \frac{P^2}{2} \frac{dC}{dA} \rightarrow \frac{P^2}{2} \frac{\Delta C(D/f)}{\Delta A} = \sigma^2 t_c \frac{Y_c^2(D/f)}{E_0} \quad (11)$$

where $Y_c(D) = \sqrt{2\psi(D/2) - \psi(D)}$ is a dimensionless calibration function. Importantly, G_m is found by *discrete* differentiation of compliance, $C(D) = f / (D(t_c + t_s)W E_{eff}(D/f))$, and finite area due to formation of a complete coating crack ($\Delta A = t_1 W$). Alternative models that treat D as a continuous variable give poor results [35]. Predicted failure strain as a function of crack density becomes:

$$\varepsilon_{max}(D) = \frac{\sigma_{max}(D)}{E_{eff}(D)} = \frac{\sqrt{G_{mc} E_0}}{E_{eff}(D) Y_c(D/f) \sqrt{t_c}} \quad (12)$$

¹Equation (10) is derived from Eq. (21) in Ref. [39] by defining $\psi(D) = 2C_3 E_c^2 \chi(\rho) / E_0$ where $\rho = 1/(2t_c D)$ is a dimensionless crack spacing, C_3 is constant with units 1/pressure, and $\chi(\rho)$ is dimensionless function derived from solution to a 4th order differential equation that minimizes complementary energy.

where G_{mc} is the coating's cracking toughness. which is assumed to be a thickness-independent, material property. This finite fracture mechanics result is analogous to the conventional fracture mechanics result in Eq. (7). Crack-length scaling in conventional fracture is replaced by coating thickness scaling in finite fracture mechanics. The $\sqrt{t_c}$ in the denominator explains why initial cracking strain decreases as coating thickness increases.

Finite fracture mechanics predictions were compared to ADaM simulations. The finite fracture mechanics modeling needed three material properties — G_{mc} , f , and $E_c(\varepsilon_i)$. Like G_{Ic} vs. $G_{Ic}^{(d)}$ for crack propagation, G_{mc} is expected to be different, and higher, than $G_{Ic}^{(d)} = 100 \text{ J/m}^2$ used in ADaM simulations. The parameter f can refine fits, but should remain between 1.25 and 1.5. Finally $E_c(\varepsilon_i)$ is coating modulus at the onset of cracking where ε_i is strain to initiate cracking (which is always greater than ε_n to initiate damage). In linear-elastic, finite fracture mechanics modeling, E_c is simply the coating modulus [31, 39]. But that analysis is predicting energy associated with cracks forming in an undamaged coating. The ADaM simulations show that damage accumulates prior to the first crack. Because fits using undamaged coating modulus did not work well, $E_c(\varepsilon_i)$ was adjusted to account for damage. From the average stiffness seen in ADaM modeling with a 2 mm coating prior to any coating cracking, the effective modulus of the damaged coating was estimated as $E_c(0.40\%) = 3.4 \text{ GPa}$. By Eq. (12), initiation strain decreases for thicker coatings suggesting less damage at initiation or that $E_c(\varepsilon_i)$ should increase with $\sqrt{t_c}$. The coating modulus at initiation was therefore assumed to be $E_c(\varepsilon_i) = 3.4\sqrt{3/2} = 4.16 \text{ GPa}$ and $E_c(\varepsilon_i) = 3.4\sqrt{4/2} = 4.81 \text{ GPa}$ for 3 and 4 mm coatings, respectively. In brief, finite fracture mechanics modeling was fit to ADaM simulations by varying G_{mc} for values greater than 100 J/m^2 , keeping f between 1.25 and 1.5, and fixing $E_c(\varepsilon_i)$ to values determined above. These G_{mc} and f parameters were assumed to be thickness-independent material properties. The finite fracture mechanics fits are the solid lines in Fig. 7 and all agreed well with the ADaM simulations. The finite fracture mechanics properties were $G_{mc} = 500 \text{ J/m}^2$ and $f = 1.4$. The ADaM simulations are consistent with finite fracture mechanics models and both are consistent with experiments on cracking of coatings.

4. Conclusions

Direct comparisons of damage mechanics simulations to fracture mechanics modeling with explicit cracks on the same problem within the same code has revealed both the potential power of damage mechanics and significant pitfalls of damage mechanics modeling if done incorrectly. Some key conclusions are:

1. Damage mechanics implementation must use anisotropic damage mechanics [6, 7, 8, 9]. Anisotropic features are needed to partition loading into tensile and shear modes for modeling of mixed-mode failure and to handle crack contact. Isotropic (or scalar) damage mechanics has no sensible means for either partitioning dissipated energy or tracking crack opening displacements.
2. Damage mechanics properties for initiation stress and toughness require calibration to match fracture mechanics predictions. The toughness is always lower than observed toughness. Initiation stress for damage differs from experimental stress at failure. If suitable damage mechanics properties are selected, damage mechanics works well.

3. Damage mechanics initiation stress is not a material property because it must scale with material point size (or element size in FEA). This scaling would extend to simulations with variable-sized material points (or elements) within a single simulation where initiation stress must be different for each particle (or element). The damage mechanics toughness is relatively insensitive to scaling and therefore a material property, albeit one that differs from experimental material toughness.
4. If anisotropic damage mechanics only reproduced fracture mechanics, it would be uninteresting. The simulations of periodic cracks in coatings that combined initiation and propagation show that anisotropic damage mechanics has potential in problems where fracture mechanics is unsuitable.

Acknowledgement—This work was made possible by the endowment for the Richardson Chair in Wood Science and Forest Products.

References

- [1] E. F. Rybicki, M. F. Kanninen, A finite element calculation of stress intensity factors by a modified crack closure integral, *Eng. Fract. Mech.* 9 (1977) 931–938.
- [2] J. R. Rice, A path independent integral and the approximate analysis of strain concentration by notches and cracks, *J. Applied Mech.* June (1968) 379–386.
- [3] L. Kachanov, Time of rupture process under creep conditions, *Izv. Akad. Nauk SSR, Otd. Tekh. Nauk* 8 (1958) 26–31.
- [4] J. Oliver, Modelling strong discontinuities in solid mechanics via strain softening constitutive equations. Part 2: Numerical simulation, *International Journal for Numerical Methods in Engineering* 39 (21) (1996) 3601–3623.
- [5] J. Oliver, Modelling strong discontinuities in solid mechanics via strain softening constitutive equations. Part 1: Fundamentals, *International Journal for Numerical Methods in Engineering* 39 (21) (1996) 3575–3600.
- [6] J.-L. Chaboche, Development of continuum damage mechanics for elastic solids sustaining anisotropic and unilateral damage, *International Journal of Damage Mechanics* 2 (4) (1993) 311–329.
- [7] J. Chaboche, Le concept de contrainte effective appliqué à l'élasticité et à la viscoplasticité en présence d'un endommagement anisotrope, in: J.-P. Boehler (Ed.), *Mechanical Behavior of Anisotropic Solids / Comportement Mécanique des Solides Anisotropes*, Springer Netherlands, 1979, pp. 737–760.
- [8] J. Chaboche, Anisotropic creep damage in the framework of continuum damage mechanics, *Nuclear Engineering and Design* 79 (3) (1984) 309 – 319.
- [9] J. A. Nairn, C. C. Hammerquist, Y. E. Aimene, Numerical implementation of anisotropic damage mechanics, *Int. J. for Numerical Methods in Engineering* 112 (12) (2017) DOI:0.1002/nme.5585.
- [10] J. A. Nairn, Material point method calculations with explicit cracks, *Computer Modeling in Engineering & Sciences* 4 (2003) 649–664.
- [11] D. Sulsky, Z. Chen, H. L. Schreyer, A particle method for history-dependent materials, *Comput. Methods Appl. Mech. Engrg.* 118 (1994) 179–186.
- [12] S. G. Bardenhagen, E. M. Kober, The generalized interpolation material point method, *Computer Modeling in Engineering & Sciences* 5 (2004) 477–496.
- [13] J. A. Nairn, Numerical implementation of imperfect interfaces, *Computational Materials Science* 40 (2007) 525–536.
- [14] J. A. Nairn, Modeling of imperfect interfaces in the material point method using multimaterial methods, *Computer Modeling in Eng. & Sci.* 92 (3) (2013) 271–299.
- [15] J. A. Nairn, Analytical and numerical modeling of R curves for cracks with bridging zones, *Int. J. Fract.* 155 (2009) 167–181.

- [16] Y. Guo, J. A. Nairn, Calculation of j-integral and stress intensity factors using the material point method, *Computer Modeling in Engineering & Sciences* 6 (2004) 295–308.
- [17] Y. Guo, J. A. Nairn, Three-dimensional dynamic fracture analysis in the material point method, *Computer Modeling in Engineering & Sciences* 16 (2006) 141–156.
- [18] T. Belytschko, T. Black, Elastic crack growth in finite elements with minimal remeshing, *Int. J. for Numerical Methods in Engineering* 45 (1999) 601–620.
- [19] N. Moës, J. Dolbow, T. Belytschko, A finite element method for crack growth without remeshing, *Int. J. for Numerical Methods in Engineering* 46 (1999) 131–150.
- [20] F. Erdogan, G. C. Sih, On the crack extension in plates under plane loading and transverse shear, *Journal of Basic Engineering*, ASME 85 (1963) 519–527.
- [21] A. G. Atkins, Y. W. Mai, *Elastic and Plastic Fracture*, John Wiley & Sons, New York, 1985.
- [22] J. G. Williams, *Fracture Mechanics of Polymers*, John Wiley & Sons, New York, 1984.
- [23] K. Ravichandran, A. Vasudevan, *ASM Handbook, Volume 19: Fatigue and Fracture*, ASM International, 1996, Ch. Fracture Resistance of Structural Alloys, pp. 381–392.
- [24] J. A. Nairn, Generalized crack closure analysis for elements with arbitrarily-placed side nodes and consistent nodal forces, *Int. J. Fracture* 171 (2011) 11–22.
- [25] T. Shimada, K. Ouchi, Y. Chihara, T. Kitamura, Breakdown of continuum fracture mechanics at the nanoscale, *Scientific Reports* 5 (2015) 8596 EP.
- [26] J. F. Kalthoff, Transition in the failure behavior of dynamically shear loaded cracks, *ASME. Appl. Mech. Rev.* 43 (5S) (1990) S247–S250.
- [27] J. F. Kalthoff, S. Winkler, Failure mode transition at high rates of shear loading, 1987, pp. 185–195.
- [28] R. C. Batra, M. V. S. Ravinsankar, Three-dimensional numerical simulation of the kalthoff experiments, *Int. J. Fract.* 105 (2000) 161–186.
- [29] S. Li, W. K. L. and A. J. Rosakis, T. Belytschko, W. Hao, Mesh-free galerkin simulaitons of dynamic shear band propagation and failure mode transition, *Int. J. Solids Structures* 39 (2002) 1213–1240.
- [30] S. Raymond, V. Lemiale, R. Ibrahim, R. Lau, A meshfree study of the halthoff-winkler experiment in 3d at room and low temperatures under dynamic loading using viscoplastic modeling, *Engineering Analysis with Boundary Elements* 42 (2014) 20–25.
- [31] J. A. Nairn, S. R. Kim, A fracture mechanics analysis of multiple cracking in coatings, *Engr. Fract. Mech.* 42 (1992) 195–208.
- [32] Y. Leterrier, L. Boogh, J. Andersons, J.-A. E. Månson, Adhesion of silicon oxide layers on poly(ehtylene terephthalate). I: Effect of substrate properties on coating's fragmentation process, *J. Polym. Sci., Part B: Polymer Physics* 35 (1997) 1449–1461.
- [33] Y. Leterrier, J. Andersons, Y. Pitton, J.-A. E. Månson, Adhesion of silicon oxide layers on poly(ehtylene terephthalate). II. effect of coating thickness on adhesive and cohesive strengths, *J. Polym. Sci., Part B: Polymer Physics* 35 (1997) 1463–1472.
- [34] S. R. Kim, J. A. Nairn, Fracture mechanics analysis of coating/substrate systems subjected to tension or bending loads II: Experiments in bending, *Engr. Fract. Mech.* 65 (2000) 595–607.
- [35] J. A. Nairn, S. Hu, J. S. Bark, A critical evaluation of theories for predicting microcracking in composite laminates, *J. Mat. Sci.* 28 (1993) 5099–5111.
- [36] J. A. Nairn, S. Hu, *Damage Mechanics of Composite Materials*, Elsevier, Amsterdam, Ed. Ramesh Talreja, 1994, Ch. Micromechanics of Damage: A Case Study of Matrix Microcracking, pp. 187–243.
- [37] J. A. Nairn, *Comprehensive Composite Materials, Vol. 2*, Elsevier Science, Ed. R. Talreja and J.-A. E. Månson, 2000, Ch. Matrix Microcracking in Composites, pp. 403–432.
- [38] Z. Hashin, Finite thermoelastic fracture criterion with application to laminate cracking analysis, *Journal of the Mechanics and Physics of Solids* 44 (1996) 1129–1145.
- [39] S. R. Kim, J. A. Nairn, Fracture mechanics analysis of coating/substrate systems subjected to tension or bending loads I: Theory, *Engr. Fract. Mech.* 65 (2000) 573–593.